ISSN 0036-0236, Russian Journal of Inorganic Chemistry, 2024. © Pleiades Publishing, Ltd., 2024.

THEORETICAL
INORGANIC CHEMISTRY

Electronic Structure of Cobalt Phosphates $Co_{1-x}M_xPO_4$ Doped with Iron and Nickel Atoms

M. D. Pecherskaya[a], *, O. A. Galkina[b], O. N. Ruzimuradov[c], and Sh. I. Mamatkulov[a]

[a] *Institute of Materials Science, Uzbekistan Academy of Sciences, Tashkent, 100084 Uzbekistan*

[b] *Institute of Chemistry and Physics of Polymers, Uzbekistan Academy of Sciences, Tashkent, 100128 Uzbekistan*

[c] *Turin Polytechnic University in Tashkent, Tashkent, 100095 Uzbekistan*

**e-mail: mariya.pecherskaya@yahoo.com*

Received October 19, 2023; revised February 13, 2024; accepted February 17, 2024

Abstract—In this research, the electronic states, band structures, and bond properties of the framework compounds of $CoPO_4$, $Co_{1-x}Fe_xPO_4$, and $Co_{1-x}Ni_xPO_4$ were investigated by the density functional theory calculations. The potential capabilities of these systems in the photocatalytic water splitting to produce hydrogen were analyzed. The spin-up electron densities of states for the $CoPO_4$, $Co_{1-x}Fe_xPO_4$, and $Co_{1-x}Ni_xPO_4$ systems have band gaps of 2.7, 3.4, and 3.45 eV, respectively. The band of spin-down electron states has several energy gaps above the Fermi level. The density of states of electron with spin up near the Fermi level is obviously greater than that of electrons with spin down. In this case, localized states of electrons appear in the band gap of doped semiconductors due to impurity atoms. The calculated value of the energy at the lower edge of the conduction band for $CoPO_4$ was –0.7 eV, which is more negative than the energy required for water splitting. Meanwhile, the calculated value of the energy at the upper edge of the valence band was 2.01 eV, which is more positive than the oxygen evolution energy of 1.23 eV.

Keywords: Fe and Ni doped cobalt phosphate, density functional theory, band gap, electronic characteristics

DOI: 10.1134/S0036023624600540

INTRODUCTION

Recently, with the rapid development of hydrogen energy, more and more attention is being paid to producing hydrogen in an environmentally friendly way using water photolysis. Of particular interest is the development of low-cost photocatalysts for the dissociation of water (to hydrogen and oxygen) under the influence of sunlight.

Various semiconductor materials based on transition metals, such as oxides, have found wide application as photocatalysts [1–3], hydroxides [4], sulfides [5], nitrides [6], selenides [7], borides [8], chalcogenides [9], and phosphides/phosphates [10]. However, despite their high chemical inertness, environmental friendliness and low manufacturing cost, many of them have a number of significant disadvantages. Namely, they need to satisfy the basic requirements for an effective photocatalytic process, such as (i) from the point of view of thermodynamics, the upper edge of the valence band of the semiconductor should be located more positively than the redox potential of the O_2/H_2O pair (+1.23 V relative to normal hydrogen electrode (NHE) at pH 0), and the lower edge of the conduction band should be positioned more negative than the H^+/H_2 reduction potential (0 V relative to NHE at pH 0). Therefore, the minimum photon energy thermodynamically required to excite the reaction is 1.23 eV; (ii) band gap (E_g) of the semiconductor determines the spectrum of action of the photocatalyst; the smaller the value of E_g, the more long-wavelength light is available for absorption. For example, to absorb visible light E_g should be < 3 eV, and the most wide-gap photocatalysts exhibit activity only under UV irradiation. There are a number of other important conditions for the effective occurrence of the photocatalytic water decomposition, which is fundamental in the search for new photocatalysts for the release of oxygen and hydrogen [11].

Recently, new transition metal phosphate/phosphide-based materials have been intensively studied due to their most efficient catalytic activity in the hydrogen evolution reaction, as well as their exceptional activity and stability. In addition, the study of phosphates with a framework structure results from their high chemical and radiation resistance and the ability to incorporate (dope) cations of different charges and sizes into the crystal structure. In particular, prospects for the development of transition metal phosphates for oxygen evolution reactions (OER) with high performance have been reported [12, 13]. The ability to incorporate various alkali metals into a poorly soluble stable structure is an important advan-

tage of frame structure phosphates. The introduction of transition metals into framework phosphates makes it possible to develop cheaper monophasic matrices and materials with the required properties.

Synthesis of electrocatalyst (Co, Fe)PO_4 based on the phosphate method for the hydrogen evolution reaction (HER) in the alkaline splitting of seawater is reported [14]. (Co,Fe)PO_4 demonstrates high activity and longevity of HER in alkaline natural seawater (1 M KOH + seawater), providing a current density of 10 mA/cm^2 at an excess potential of 137 mV. In addition, the measured potential of the electrocatalyst (Co, Fe)PO_4 at constant current density 100 mA/cm^2 remains highly stable without noticeable degradation over 72 h of continuous operation in alkaline natural seawater, indicating its suitability for seawater applications. Notably, iron phosphate doped with cobalt and nickel provides the best electrochemical water splitting performance in terms of HER, OER, and total water splitting. Transition metal doping significantly increases catalytic activity, providing high current densities and low excess potentials due to improved electrical conductivity and the process of activating partial charge transfer from metal to metal. In addition, doping leads to changes in the crystal structure and morphology of the final photocatalyst. Mesoporosity and the synergistic interaction of both metal atoms result in improved performance compared to pure iron phosphate. Compounds having metal atoms in a higher valence state lead to the formation of intermediates that are highly adsorbed on the surface. During long-term catalysis, a transition of Co^{2+} and Fe^{2+} states into states with a higher oxidation state occurs. The results of spectroscopic studies indicate that the active state of the catalyst consists of clusters with mixed valence $Co^{2+/3+}$ and $Fe^{2+/3+}$. The transition from a crystalline to an amorphous mesoporous structure, the synergistic interaction of the metals Co and Fe, as well as the electronic transition to higher states lead to a significant increase in the efficiency of the overall decomposition of water.

The authors [15] have studied the photoelectrochemical characteristics of the heterogeneous $Co_3(PO_4)_2$ system modified with reduced graphene oxide (RGO) in the hydrogen evolution reaction. In particular, it is shown that $Co_3(PO_4)_2$ anchored on RGO nanosheets exhibits enhanced photocatalytic activity. It was noted that the increase in photoactivity is mainly due to the stepped type II heterojunction system, in which photoinduced electrons from the three-dimensional $Co_3(PO_4)_2$ switch to two-dimensional RGO and lead to a decrease in charge recombination, which is confirmed by photoluminescence spectroscopy data. The bandgap value of $Co_3(PO_4)_2$ was calculated using the Kubelka–Munk method to be equal to 2.35 eV. Unfortunately, catalysts based on cobalt compounds, including $CoPO_4$, remain relatively little studied from the point of view of photocatalytic hydrogen evolution, despite the fact that they are effective light-trapping materials and act as strong electron mediators [16–18].

On the other hand, the attractiveness of compounds with phosphate groups is due to the presence of an inductive effect and the provision of good ionic conductivity due to the emergence of channels between bulky PO_4^{3-} groups. The absence of long-range order in amorphous semiconductors can lead to the formation *in-gap* electronic states in the band gap associated with defects or doped elements that correspond to an intrinsic property of a disordered material [19]. The ability of transition metal phosphate compounds to carry out redox reactions on their surface depends on the size of the band gap relative to the free energies of the reactions of interest. Reactions are thermodynamically favorable if their free energies are located in the band gap energy. Therefore, it is very important to have an understanding of the electronic structure of transition metal phosphate compounds.

In this work, using the density functional theory method (DFT) within the framework of the local density approximation, electronic states, band structures, bonding properties, the electronic conductivity of $CoPO_4$,$Co_{1-x}Fe_xPO_4$, and $Co_{1-x}Ni_xPO_4$ framework compounds were studied. The band gap of the structures under study was determined, and the ability of these compounds to carry out redox reactions was analyzed. The results show that band structures $Co_{1-x}M_xPO_4$ are anisotropic. The band gap for spin-up electronic states is different from that of spin-down electronic states, which have multiple energy gaps above the Fermi level. The density of states of electrons with spin up near the Fermi level is obviously higher than that of electrons with spin down.

COMPUTATION DETAILS

Calculations of the electronic structure of cobalt phosphate were performed within the framework of the local density functional theory LDA + U [20], taking into account monatomic Coulomb correlations and exchange, using the Quantum Espresso software package [21]. Adsorption energies and spin-dependent band centers were calculated within DFT using the exchange-correlation functional with the Perdue–Burke–Ernzerhoff parameterization based on the generalized gradient approximation (GGA LDA). The wave functions were expanded into plane waves and limited to an energy of 400 eV. To optimize the geometry and calculate the electronic structure of the systems under study, we used a supercell consisting of 48 atoms and a Monkhorst–Pack grid with 8 × 8 × 8 k-dots (Fig. 1). The following electronic configurations were used in the calculation: for Co atoms, [Ar]$4s^24p^03d^7$; for P atoms, [Ne]$3s^23p^3$; for O atoms, [He]$2s^22p^4$; for Ni atoms, [Ar]$4s^24p^03d^8$; for Fe atoms,

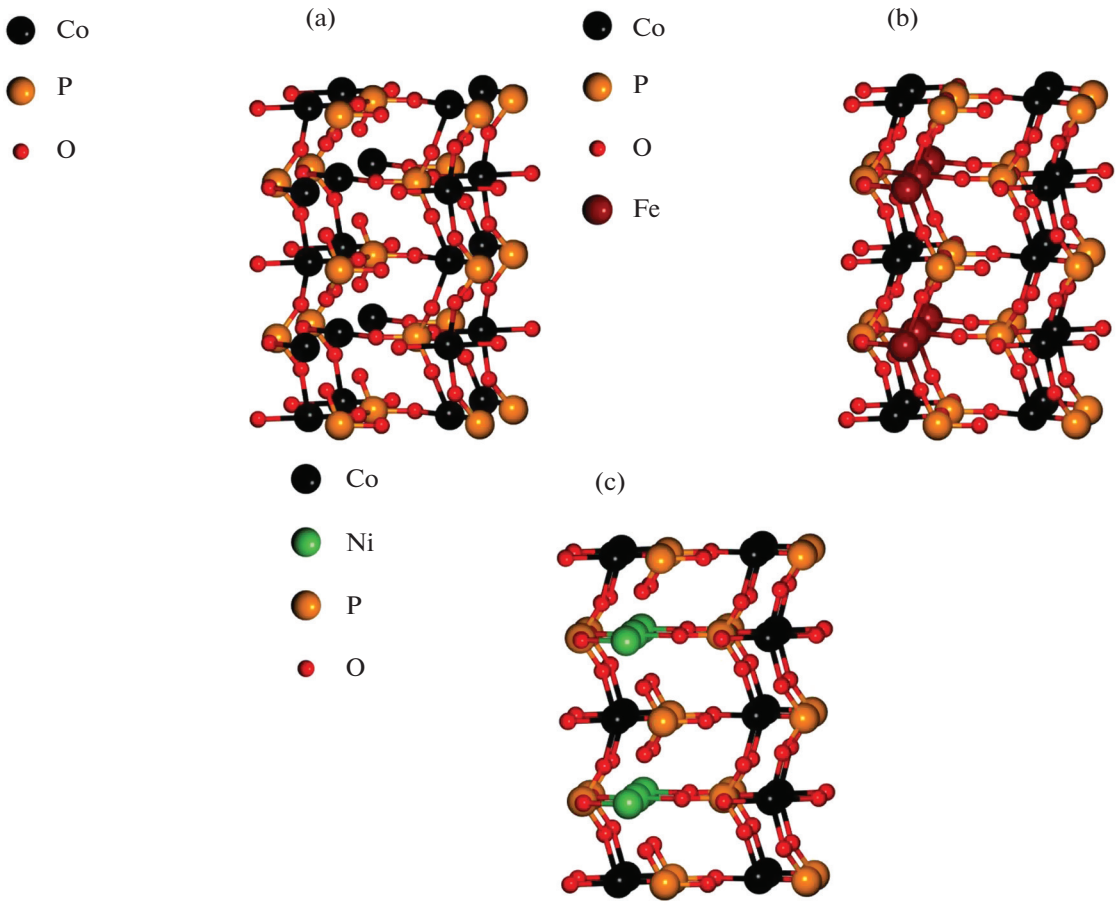

Fig. 1. Crystal structures of (a) $CoPO_4$, (b) $Co_{1-x}Fe_xPO_4$, and (c) $Co_{1-x}Ni_xPO_4$ used in the calculations. Oxygen, phosphorus, and cobalt atoms are indicated in red, yellow, and dark green, respectively.

[Ar]$4s^2 3d^6$. Electrons in a completely filled [Ar, Ne, He] shell were assigned to the core. The influence of valence electrons was taken into account by using ultrasoft (ultrasoft Vanderbilt) pseudopotentials. Atomic positions and cell parameters of pure $CoPO_4$ were optimized by the quasi-Newton method using the BFGS (Broyden–Fletcher–Goldfarb–Shanno) algorithm to force reductions within 0.01 eV/Å for unconstrained atoms and were compared with experimental data. Lattice Dimensions of Pure $CoPO_4$ obtained by the LDA + method U are shown in Table 1. Calculation data $a = 9.28$ Å, $b = 5.11$ Å, $c = 4.25$ Å satisfactorily coincide with the experimental lattice values obtained [22], where $a = 9.58$ Å, $b = 5.79$ Å, $c = 4.77$ Å. In optimized $CoPO_4$ geometry, cobalt atoms were replaced by iron or nickel atoms and were also optimized using the BFGS algorithm.

The main error in semiconductor calculations using the electron density functional theory method is the well-known underestimation of the band gap. To compensate for this error, we used the method of introducing single-center Hubbard corrections to U-Coulomb and J-exchange interactions in atoms (LDA + U). Parameter U used in this calculation method is an empirically selected value, and parameter J, characterizing the exchange interaction, was taken equal to

Table 1. Unit cell parameters for $Co(PO_4)$, $Co_{1-x}Fe_xPO_4$, and $Co_{1-x}Ni_xPO_4$ ($x = 0.05$) calculated using the LDA + U method and experimental data for comparison

Unit cell parameter, Å	$Co(PO_4)$	$Co_{1-x}Fe_xPO_4$	$Co_{1-x}Ni_xPO_4$	Experiment [22]
a	**9.28**	9.58	9.55	**9.58**
b	**5.11**	5.01	5.03	**5.79**
c	**4.25**	4.21	4.15	**4.77**

Table 2. Values of band gap and magnetic moments of $Co(PO_4)$, $Co_{1-x}Fe_xPO_4$, and $Co_{1-x}Ni_xPO_4$ at $x = 0.05$ in various Hubbard correction values

Method	U_{Co3d}	J_{Co3d}	E_g	E_{CB}	E_{VB}	μ_B
	eV					
$Co(PO_4)$/LDA	0	0	0.4	–	–	0.0
$Co(PO_4)$/LDA	4.0	2.0	2.5	–	–	2.7
$Co(PO_4)$/LDA	5.0	2.0	2.7	−0.69	2.01	2.98
$Co_{1-x}Fe_xPO_4$/LDA	5.0	2.0	3.4	−0.32	3.08	2.97
$Co_{1-x}Ni_xPO_4$/LDA	5.0	2.0	3.45	−0.32	3.13	2.95
Experiment [22]			2.7			3.1

2 eV for all calculations performed [23, 24]. By varying combinations of parameters U and J a series of calculations was carried out in order to obtain the experimentally observed value of the band gap for pure $CoPO_4$, which amounted to 2.7 eV. For different parameter values U, the values of the band gap and spin magnetic moment for the cobalt atom were found. These results, as well as the values experimentally obtained by the authors [27, 28], are present in Table 2. Thus, for the cobalt atom we used the values of U and J equal to 5.0 and 2.0 eV, respectively.

In this work, various structures of cobalt phosphates were considered, including monoclinic and orthorhombic crystal symmetries. All studied structures are taken from the Materials Project database [25]. Although on the Materials project website orthorhombic $CoPO_4$ structures with symmetries $Pna2_1$ and *Pnma* designated as not experimentally detected, nevertheless in the works [22, 26] $CoPO_4$ structures with symmetries $Pna2_1$ and *Pnma* have been studied doped with lithium atoms. In Figs. 1a–1c, the geometry of both pure cobalt phosphate and Fe- or Ni-doped cobalt phosphate is shown. Crystal structure of $CoPO_4$ described by a unit cell belonging to orthorhombic symmetry $Pna2_1$ and contains 24 basic atoms. The lattice constants for the studied systems are given in Table 1. Co atoms in the structure of $CoPO_4$ are sixfold coordinated by O atoms, moreover, in such a way that there are three nearest O atoms at a distance of 1.85 Å, and three next to the nearest O atoms at a distance of 1.98 Å, while P atoms have tetrahedral coordination. Simulation of doped $CoPO_4$ was performed by replacing one of the cobalt atoms with nickel and iron atoms of a $2 \times 1 \times 1$ supercell consisting of 48 atoms obtained by double translation of the $CoPO_4$ unit cell along x-translation vector. In calculations we used the crystal structures of $Co_8(PO_4)_8$,$Co_7Fe(PO4)_8$, and $Co_7Ni(PO_4)_8$, which correspond to ~5% doping of pure $Co_8(PO_4)_8$ with iron and nickel atoms (Fig. 1).

RESULTS AND DISCUSSION

Structure of $CoPO_4$ Energy Zones

Figures 2a–2d show a comparative study of partial densities of electronic states for electrons with up and down spins for $Co(PO_4)$ and Fe- and Ni-doped $Co(PO_4)$. O2*p* and Co3*d* wave functions are highly localized, and the O2*p* states are energetically very close to Co3*d* states, which indicates a significantly strong interaction between O2*p* and Co3*d*. Upper levels of the $Co(PO)_4$ valence band can be decomposed into three main regions, and there are five minority spin states: bonding states σ formed by O*p* bonds; in the middle there are binding states t_{1u}; and at the top there are antibinding O$p\pi$*-states where hybridization with t_{2g}-electrons Co is insignificant. Density of spin-up electron levels in the valence band $Co(PO_4)$ DOS is absent from approximately −18.14 to −13 eV and uniformly distributed from −13 eV to 0 eV. Levels in the conduction band are uniformly distributed up to 8 eV. Band gap for spin-up electrons $E_g^u = 2.7$ eV. The DOS distribution for spin-down electrons in the valence band is much smaller near the Fermi level, extending from approximately −12.5 to −1.0 eV, and there is a small unoccupied state near the Fermi level from −1.1 eV. In the case of spin-down electrons, the band gap has the values $E_g^d = 2.31$ eV, and in the middle of the bandgap local vacant electronic states appear mainly due to *d* levels of the cobalt atom.

Figures 2c, 2d show the densities of electronic states for $Co_{1-x}Fe_xPO_4$. When cobalt phosphate is doped with iron atoms, the band gap increases slightly compared to pure $CoPO_4$ and reaches up to 3.4 eV for electrons with the dominant spin direction. Levels of the electron band $Co_{1-x}Fe_xPO_4$ consist of five main regions, where there are four minority spin states. In the spectrum of the density of electronic states with spin up and down, vacant *d*-orbital states of the Fe atom are formed in the band gap.

Figures 2d, 2e show the densities of electronic states for $Co_{1-x}Ni_xPO_4$. When cobalt phosphate is

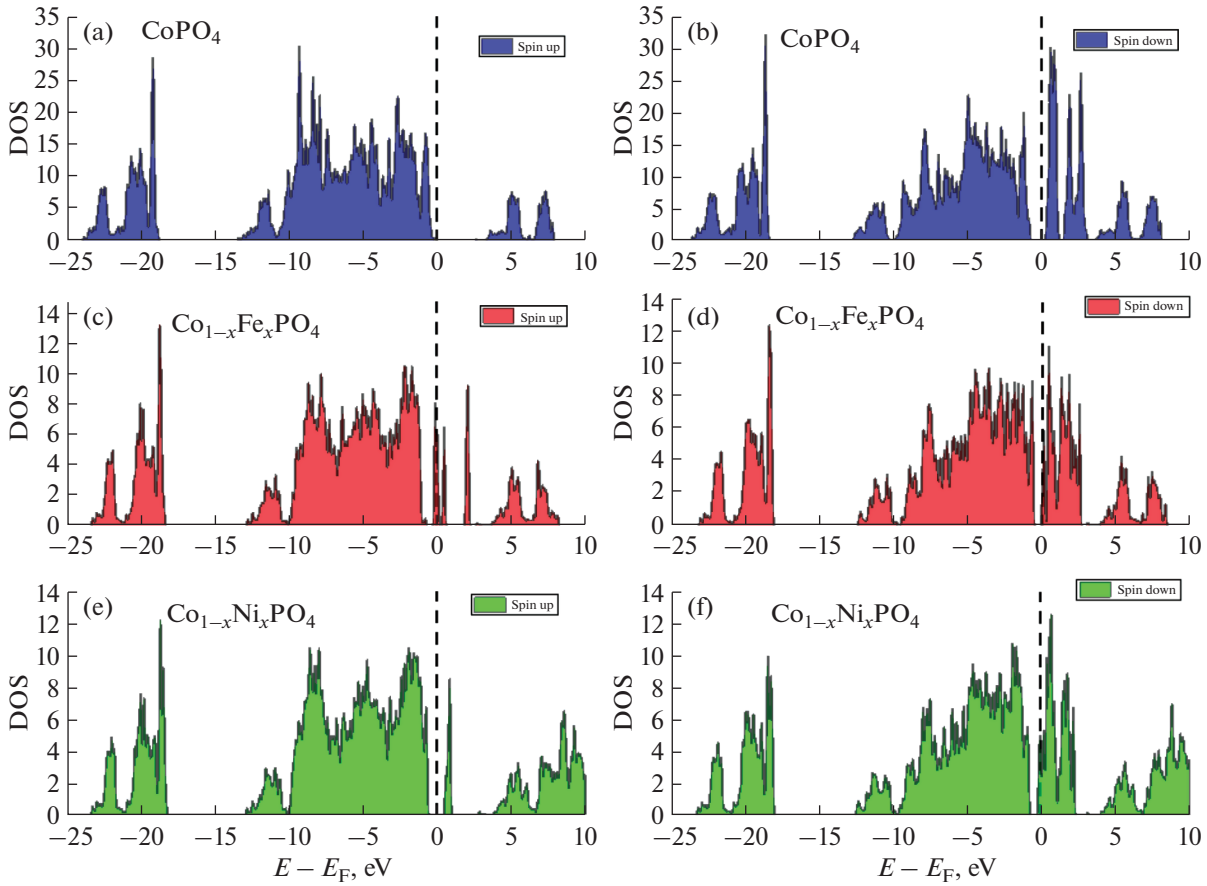

Fig. 2. Density of states (DOS) with spin up and spin down for pure $CoPO_4$ (a, b), as well as $CoPO_4$ alloyed with (c, d) iron and (e, f) nickel. Zero-point energy is taken at the Fermi level, the left half of the figures represents the spin-up state, and the right half represents the spin-down state.

doped with nickel atoms, the band gap slightly increases, as in the case of doping with Fe atoms, and amounts to 3.45 eV for electrons with the dominant spin direction. In the band gap, several localized electronic levels are observed, where Ni atoms participate in the localization of the defect state. The formation of local electronic levels may be due to the fact that most of the dopant induces "trap states" in the middle of the band gap of the system under study, which are responsible for higher electron-hole recombination, thereby reducing the efficiency [27].

Structural Characteristics

Systematic studies have shown that the experimentally observed band gap for $CoPO_4$ can be obtained by correcting for the Co3*d* atom: $U = 5.0$, $J = 2.0$. Table 2 presents the results for the band gap and magnetic moments of cobalt phosphate at different values of the Hubbard correction parameters U and J. Values U and J were chosen to reproduce the experimentally observed magnetic moment and band gap energy. At $U = 5.0$ and $J = 2.0$ calculated value $E_g = 2.7$ eV and the effective magnetic moment of the system $CoPO_4$ obtained as 2.98μ, which completely coincides with the result of the work [22].

The DFT method detected a change in the band gap upon doping with Fe and Ni atoms. As an example, Figs. 3–5 show band structures of $CoPO_4$ and Fe- and Ni-doped $Co(PO_4)$ respectively. General view of the calculated band structure of $CoPO_4$ (Fig. 3) is in good agreement with the band structures of $CoPO_4$ previously obtained by other calculation methods [28, 29]. $CoPO_4$ is a direct-gap semiconductor with the top of the valence band and the bottom of the conduction band at the center of the Brillouin zone of the G-point. The band gap is $E_g = 2.7$ eV. Spin polarization near the Fermi level increases in the case of doping with nickel atoms (Fig. 4). Experimental values E_g for crystalline $CoPO_4$ lie in the range 2.35–2.8 eV [30, 31]. According to the experiment, the valence band of $CoPO_4$ consists of two subbands separated by an ion gap. In the standard interpretation, the lower valence band is formed 2*s*-Co orbitals with impurity of 3*s*-, 3*p* states of P. The upper valence band is formed by 3*d*-orbitals of

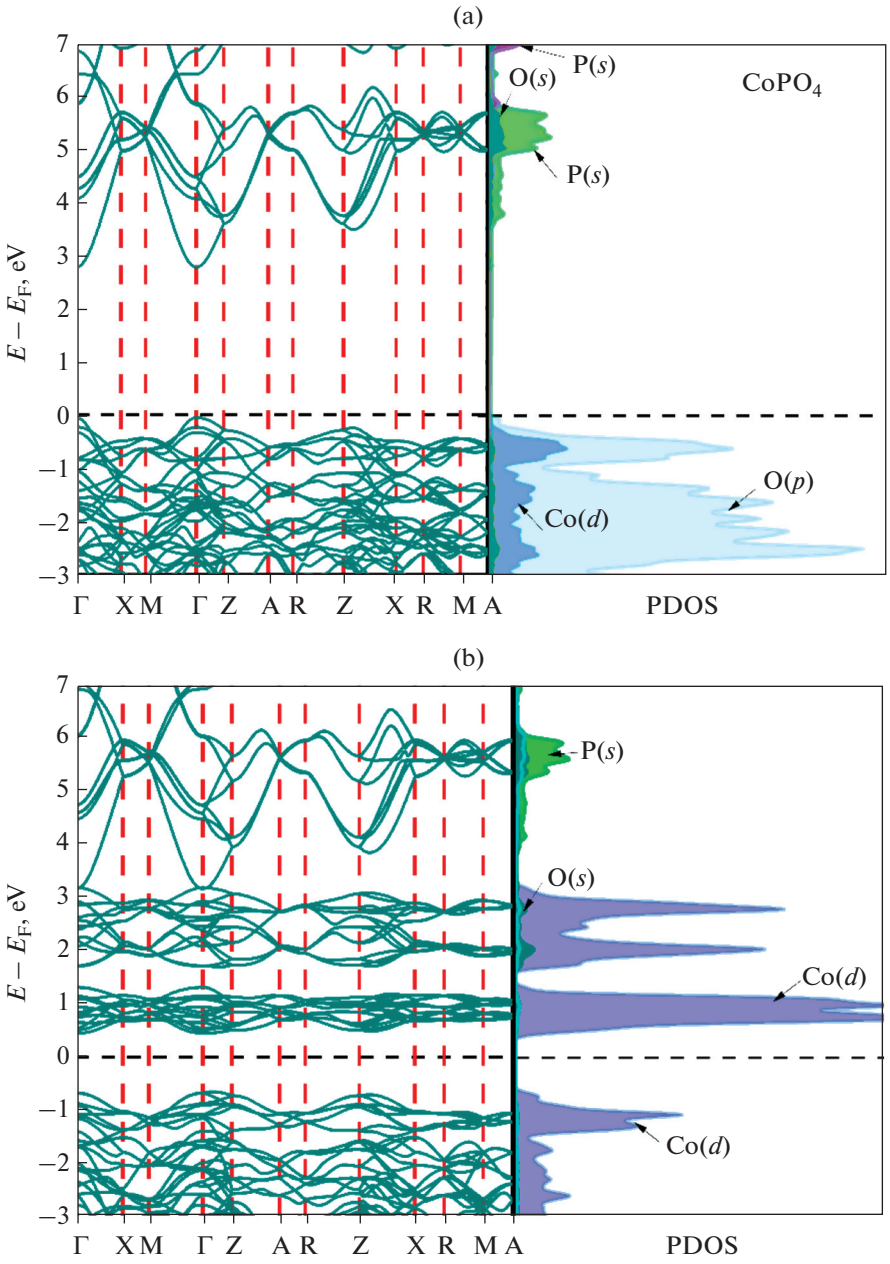

Fig. 3. Structure of energy bands and partial densities of states of the system $CoPO_4$ for (a) spin-up and (b) spin-down electrons. For this crystal, the band structures for electrons with different spin directions differ from each other, which leads to band gaps that are unequal in size and amount to $E_g^u = 2.7$ eV and $E_g^d = 1.1$ eV.

Co and 3*s*- and 3*p*-orbitals of O. In accordance with the dipole selection rules on P2*p*-level transitions from P3*s*-states are allowed (single-center local transitions).

$CoPO_4$ doping with nickel and iron atoms leads to the appearance of a set of energy levels in the energy spectrum of the crystal. Bandgap value for $Co_{1-x}Ni_xPO_4$ is equal to 3.45 eV, and for $Co_{1-x}Fe_xPO_4$ it is 3.4 eV. In particular, additional levels appear in the forbidden zone, which are filled by *d* electrons of Fe and *p*-electrons of O (Fig. 4a). Unfilled levels associated with the presence of a defect appear below the bottom of the conduction band. These local levels are located on average 0.5 eV below the bottom of the conduction band and correspond to unoccupied states.

The ability of electrons to transfer to the surface of adsorbed molecules is associated with the value of the redox potential and the position of the edges of the bands [32]. The positions of the edges of the bands were determined by absolute electronegativity and

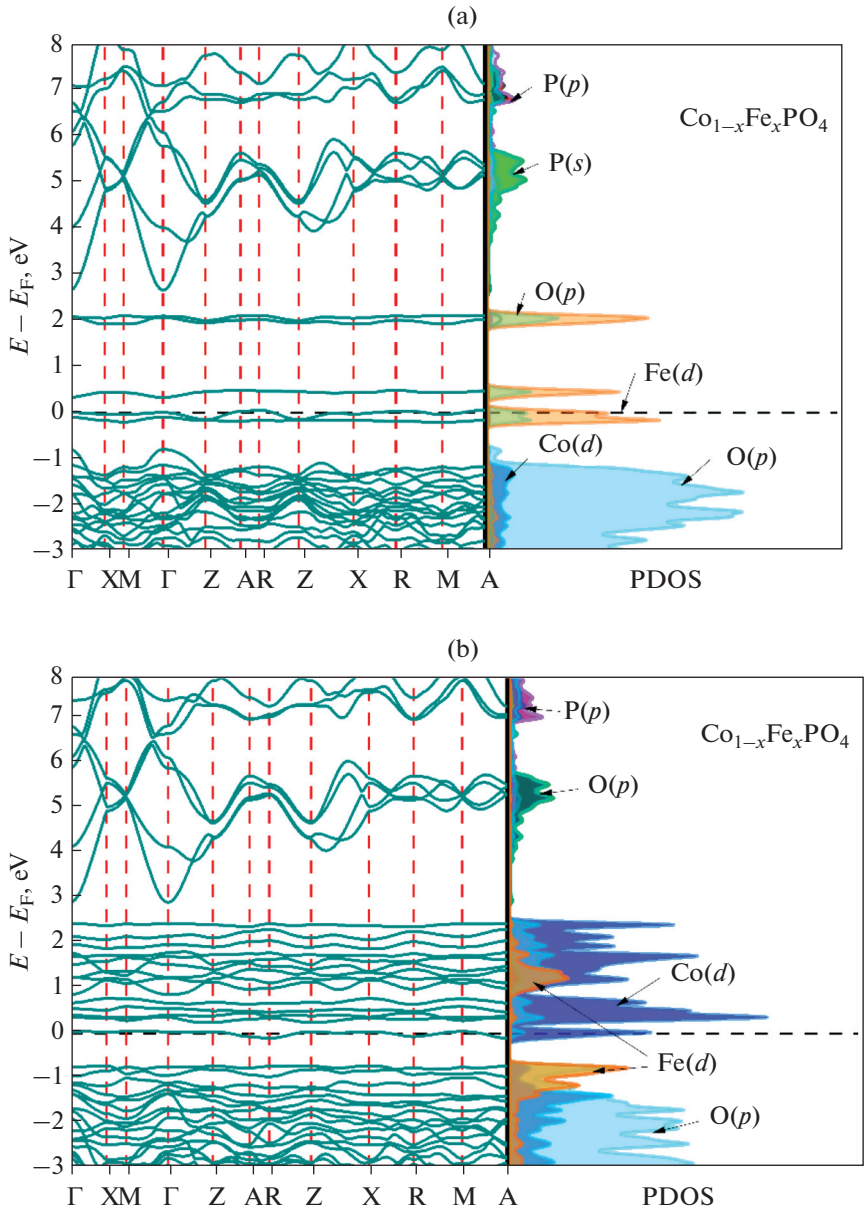

Fig. 4. Structure of energy bands and partial densities of states of system $Co_{1-x}Fe_xPO_4$ for (a) spin-up and (b) spin-down electrons.

band gap relative to the catalytic properties of photocatalysts using formulas (1) and (2) [13]:

$$E_{VB} = E_{CB} + E_g, \quad (1)$$

$$E_{CB} = -\left[\chi(A)^a \chi(B)^b \chi(C)^c\right]^{1/(a+b+c)} + E_H + 1/2E_g, \quad (2)$$

where E_{VB} and E_{CB} mean the upper edge of the valence band and the lower edge of the conduction band, respectively; χ is the geometric mean electronegativity of atoms according to Mulliken, electron free energy E_H equal to 4.5 eV on the hydrogen scale [33], and E_g is the bandgap value obtained by the LDA + U method (Table 2). Formula (2) provides the opportunity to estimate the edges of the valence band and conduction band through the electronegativity of the atoms in the system and the band gap values of the semiconductor. Research presented in the work [34] shows that the sum of this value and the band gap (ΔE) can represent the energy value of the extreme limit of the photoelectric effect, as described by Eq. (2). In other words, the value of electron affinity and electronegativity in these cases characterize the valence band of the structure. The absolute electronegativity is determined to be ~6.52 eV for all systems considered. Energy value of

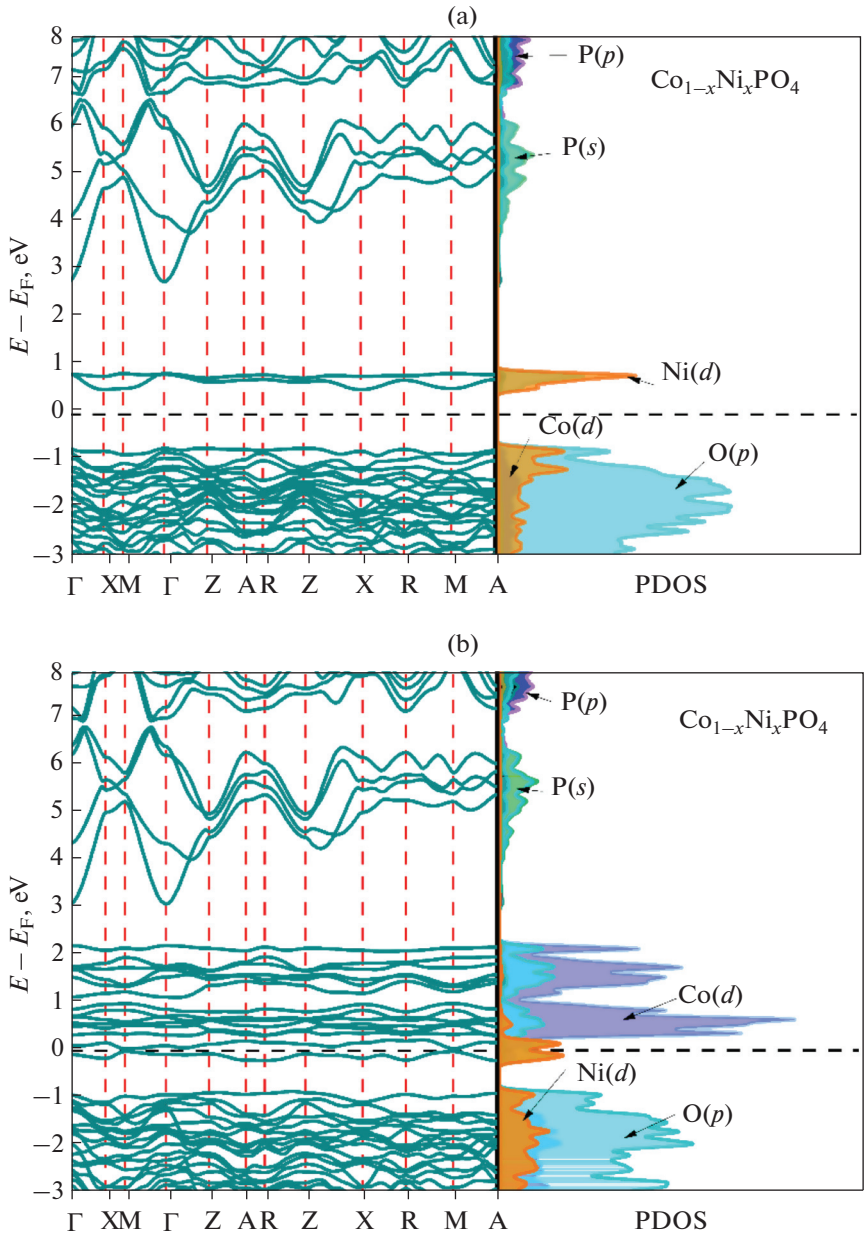

Fig. 5. Structure of energy bands and partial densities of states of the system $Co_{1-x}Ni_xPO_4$ for (a) spin-up and (b) spin-down electrons.

the lower edge of the conduction band E_{CB} for $CoPO_4$, $Co_{1-x}Fe_xPO_4$, and $Co_{1-x}Ni_xPO_4$ is −0.69, −0.32 and −0.32 eV, respectively (Table 2). This confirms that the conduction band is located more negatively than the energy of hydrogen evolution. Energy value of the upper edge of the valence band E_{VB} for these systems is 2.01, 3.13 and 3.08 eV, respectively. Based the positions of the valence and conduction bands, as well as the band gap, the systems under study can be considered suitable for the photoelectrocatalytic decomposition of water in the visible and UV light spectrum.

CONCLUSIONS

In this work, the electronic states, band structures, and bonding properties of $CoPO_4$, $Co_{1-x}Fe_xPO_4$, and $Co_{1-x}Ni_xPO_4$ crystal structures are systematically studied. The density of spin-up and spin-down electron states has different energy gaps. It has been found that the introduction of Fe and Ni atoms into the phosphate framework leads to an increase in the band gap of spin-up electronic states from 2.7 eV for pure $CoPO_4$ to 3.4 and 3.45 eV for $Co_{1-x}Fe_xPO_4$ and

$Co_{1-x}Ni_xPO_4$. In this case, localized states of electrons appear in the band gap of doped semiconductors due to impurity atoms. The calculated conduction band edge energy is positioned more negatively than the hydrogen evolution energy, and the calculated valence band top edge energy is positioned more positively than the oxygen evolution energy, which is 1.23 eV.

FUNDING

The research was carried out with the financial support of the Agency of Innovative Development under the Ministry of Higher Education, Science and Innovation within the framework of research project No. ALM-20230502808.

CONFLICT OF INTEREST

The authors of this work declare that they have no conflict of interest.

REFERENCES

1. D. Raj, F. Scaglione, G. Fiore, et al., Nanomaterials **11**, 1313 (2021). https://doi.org/10.3390/nano11051313
2. M. D. Pecherskaya, K. T. Butanov, O. N. Ruzimuradov, et al., Glass Phys. Chem. **48**, 327 (2022). https://doi.org/10.1134/S1087659622040101
3. K. Saidov, R. Shrawan, J. Razzokov, et al., E3S Web of Conferences **402**, 14038 (2023). https://doi.org/10.1051/e3sconf/202340214038
4. B. B. Gicha, L. T. Tufa, S. Kang, et al., Nanomaterials **11**, 1388 (2021). https://doi.org/10.3390/nano11061388
5. E. P. D'yachkov and P. N. D'yachkov, Russ. J. Inorg. Chem. **64**, 1152 (2019). https://doi.org/10.1134/S0036023619090080
6. X. Peng, C. Pi, X. Zhang, et al., Sustain. Energy Fuels **3**, 366 (2019). https://doi.org/10.1039/c8se00525g
7. B. Liu, Y. F. Zhao, H. Q. Peng, et al., Adv. Mater. **29**, 1606521 (2017). https://doi.org/10.1002/adma.201606521
8. Y. Jiang and Y. Lu, Nanoscale **12**, 9327 (2020). https://doi.org/10.1039/d0nr01279c
9. C. K. Sumesh and S. C. Peter, Dalton Trans. **48**, 12772 (2019). https://doi.org/10.1039/c9dt01581g
10. Z. Geng, M. Yang, X. Qi, et al., J. Chem. Technol. Biotechnol. **94**, 1660 (2019). https://doi.org/10.1002/jctb.5937
11. I. A. Rodionov and I. A. Zvereva, Russ. Chem. Rev. **85**, 248 (2016). https://doi.org/10.1070/rcr4547
12. C. Kim, S. Lee, S. H. Kim, et al., Nanomaterials **11**, 2989 (2021). https://doi.org/10.3390/nano11112989
13. A. Samal, S. Swain, B. Satpati, et al., ChemSusChem **9**, 3150 (2016). https://doi.org/10.1002/cssc.201601214
14. X. Liu, H. Lai, J. Li, et al., Photochem. Photobiol. Sciences **21**, 49 (2022). https://doi.org/10.1007/s43630-021-00139-2
15. D. A. Lutterman, Y. Surendranath, and D. G. Nocera, J. Am. Chem. Soc. **131**, 3838 (2009). https://doi.org/10.1021/ja900023k
16. M. Barroso, A. J. Cowan, S. R. Pendlebury, et al., J. Am. Chem. Soc. **133**, 14868 (2011). https://doi.org/10.1021/ja205325v
17. A. Ejsmont, A. Jankowska, and J. Goscianska, Catalysts **12**, 110 (2022). https://doi.org/10.3390/catal12020
18. J. Zhang, W. Sun, X. Ding, et al., Nanomaterials **13**, 526 (2023). https://doi.org/10.3390/nano13030526
19. Y. Surendranath, M. W. Kanan, and D. G. Nocera, J. Am. Chem. Soc. **132**, 16501 (2010). https://doi.org/10.1021/ja106102b
20. S. Lutfalla, V. Shapovalov, and A. T. Bell, J. Chem. Theory. Comput. **7**, 2218 (2011). https://doi.org/10.1021/ct200202g
21. P. Giannozzi, S. Baroni, N. Bonini, et al., J. Phys.: Condens. Matter **21**, 5502 (2009). https://doi.org/10.1088/0953-8984/21/39/395502
22. H. Ehrenberg, N. N. Bramnik, A. Senyshyn, et al., Solid State Sci. **11**, 18 (2009). https://doi.org/10.1016/j.solidstatesciences.2008.04.017
23. V. A. de la Peña O'Shea, I. Moreira, A. Roldán, et al., J. Chem. Phys. **133**, 4701 (2010). https://doi.org/10.1063/1.3458691
24. P. S. Emmeline Yeo and M. F. Ng, J. Mater. Chem. A **5**, 9287 (2017). https://doi.org/10.1039/c6ta10674a
25. A. Jain, S. P. Ong, G. Hautier, et al., APL Mater. **1**, 011002 (2013). https://doi.org/10.1063/1.4812323
26. J. Ludwig and T. Nilges, J. Power Sources **382**, 101 (2018). https://doi.org/10.1016/j.jpowsour.2018.02.038
27. S. Gahlawat, J. Singh, A. K. Yadav, et al., Phys. Chem. Chem. Phys. **21**, 20463 (2019). https://doi.org/10.1039/c9cp04132j
28. J. B. Gerken, J. G. McAlpin, J. Y. C. Chen, et al., J. Am. Chem. Soc. **133**, 14431 (2011). https://doi.org/10.1021/ja205647m
29. M. E. G. Lyons and M. P. Brandon, Int. J. Electrochem. Sci. **3**, 1386 (2008). https://doi.org/10.1016/S1452-3981(23)15533-7
30. V. Artero, M. Chavarot-Kerlidou, and M. Fontecave, Angew. Chem., Int. Ed. **50**, 7238 (2011). https://doi.org/10.1002/anie.201007987
31. C. Delmas, F. Cherkaoui, A. Nadiri, et al., Mater. Res. Bull. **22**, 631 (1987). https://doi.org/10.1016/0025-5408(87)90112-7
32. Y. P. Zhu, T. Z. Ren, and Z. Y. Yuan, Catal. Sci. Technol. **5**, 4258 (2015). https://doi.org/10.1039/c5cy00107b
33. R. G. Pearson, Inorg. Chem. **27**, 734 (1988). https://doi.org/10.1021/ic00277a030
34. Sommer A. *Photoemissive Materials: Preparation, Properties, and Uses*, Wiley, 1968.